Proceedings of the Seventh International Conference on
Railway Technology: Research, Development and Maintenance
Edited by: J. Pombo
Civil-Comp Conferences, Volume 15, Paper 9.3
Civil-Comp Press, Edinburgh, United Kingdom, 2026
ISSN: 2753-3239, doi: 10.4203/ccc.15.9.3

A Numerical–MLP-Based Framework for Rapid Prediction of EHL Pressure and Film-Thickness Profiles in Wheel–Rail Contact

Z. Dai[1,2], J. Zuo[1,2], Y. Pan[1] and J. Ding[1]

**[1]College of Transportation, Tongji University
Shanghai, China
[2]Shanghai Key Laboratory of Rail Infrastructure Durability and System Safety, Tongji University**

Abstract

Under wet rail conditions, wheel–rail adhesion is highly dependent on the normal contact behaviour at the interface, which is usually analysed using elastohydrodynamic lubrication (EHL) models. However, high-fidelity EHL calculations are time-consuming, especially when a large number of operating conditions need to be evaluated. This study proposes an MLP-based surrogate framework to predict the pressure and film-thickness distributions along the contact centreline. The training data are generated from a high-fidelity EHL model under different axle loads and train speeds, and two output-specific networks are trained separately for pressure and film thickness due to their different scales and response characteristics. Comparison with numerical results shows that the surrogate models can reproduce important response features, such as pressure peaks and film-thickness variations, with generally small errors across the majority of the parameter space. Relatively larger deviations occur in a small number of cases, mainly near the boundaries of the load–speed parameter space. In addition, the computation time is reduced from seconds to milliseconds, making the proposed framework practical for rapid wheel–rail adhesion analysis.

Keywords: wheel–rail contact, elastohydrodynamic lubrication, surrogate model, multilayer perceptron, machine learning, adhesion

1 Introduction

During railway operation, wheel–rail adhesion plays a critical role in traction, braking, and safety [1]. For dry rail conditions, experiments generally reported high adhesion levels [2–4]. Once water, oil, or other third-body media enter the contact interface, however, the adhesion coefficient may decrease markedly, thereby posing safety risks [5–6]. Since adhesion is strongly influenced by the normal contact response, especially the distributions of pressure and film thickness, it is important to study wheel–rail contact behaviour under wet conditions when analysing adhesion performance.

When the contact area is wet, the pressure within the contact patch can be high enough to induce significant pressure–viscosity effects in the interfacial medium. Under such conditions, the contact behaviour is commonly analysed within the framework of EHL theory [7]. In the EHL framework, the pressure and film thickness distributions are governed by the coupled interaction between lubricant flow and elastic deformation, with pressure-dependent lubricant properties also taken into account [8]. Because these quantities are essential for characterizing the normal contact behaviour related to wheel–rail adhesion, high-fidelity numerical EHL models have been widely used in wheel–rail adhesion studies [9–11]. However, these models are computationally expensive because the pressure field, film thickness, lubricant properties, and load balance must be solved in a strongly coupled and nonlinear manner. This makes rapid evaluation over many operating conditions difficult [8].

Machine learning has recently been applied to tribology and lubrication problems. Previous studies have shown that data-driven models can efficiently approximate EHL-related quantities, particularly film-thickness parameters [12–15]. Marian et al. [12], for example, compared several machine-learning methods for film-thickness prediction and reported improved computational efficiency while maintaining good accuracy. Issa et al. [13] used numerical data to predict central and minimum film thicknesses in elliptical EHL contacts, and their results outperformed conventional empirical formulas under complex conditions. These studies demonstrate the potential of machine learning for rapid prediction in conventional EHL applications such as gears and rolling bearings. However, rapid EHL prediction for wet wheel–rail adhesion analysis has received relatively little attention. For parametric wheel–rail adhesion analysis under wet conditions, pressure and film-thickness profiles are key quantities for characterizing the normal contact behaviour at the interface and often need to be evaluated over a range of axle-load and speed conditions. This highlights the practical value of an efficient surrogate approach for rapid evaluation of pressure and film-thickness profiles.

In this study, we develop a numerical–MLP framework for rapid prediction of pressure and film-thickness profiles in wheel–rail EHL contact. The framework is trained using a dataset generated from a high-fidelity EHL numerical model, with axle load and train speed as the main input parameters. Two separate MLP models are built for the pressure and film-thickness profiles along the contact centreline. Their predictive performance is assessed against numerical results in terms of accuracy, generalization over the parameter space, and computational efficiency.

2 Methods

2.1 Overall framework of the proposed numerical–MLP surrogate approach

Figure 1 illustrates the numerical–MLP surrogate framework used in this study. The proposed framework can be divided into two functional components: a high-fidelity numerical EHL model for data generation and an MLP-based surrogate module for rapid prediction. The numerical model generates pressure and film-thickness distributions over the selected load–speed range, while the surrogate module learns the mapping from operating parameters to the corresponding centreline profiles. Axle load and train speed are used as input parameters, while other quantities such as slip ratio and lubricant properties are kept constant. For each operating condition, the high-fidelity EHL solver first computes the pressure and film-thickness distributions of the wheel–rail EHL contact. The centreline results, together with the corresponding axle load and train speed, are then used to construct the training dataset. Because pressure and film thickness have different scales and response characteristics, two output-specific MLP surrogate models are trained separately: one for the pressure profile and the other for the film-thickness profile. Once trained, these models can rapidly predict the corresponding centreline profiles for new operating conditions without repeating the full EHL simulation. This reduces the computational cost of repeated EHL simulations while retaining the main response features.

The following sections describe the numerical model, the dataset generation procedure, and the training strategy of the surrogate models.

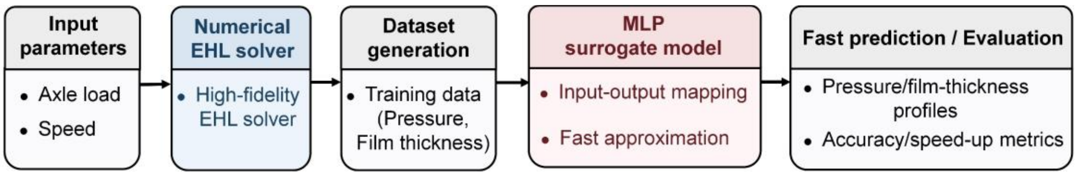

Figure 1: Schematic of the proposed numerical–MLP surrogate framework.

2.2 High-fidelity numerical EHL model

2.2.1 Governing equations

To generate training data for the surrogate model, a steady-state, isothermal, full-film point-contact EHL model is employed. The wheel–rail contact is approximated as a Hertzian elliptical contact between an ellipsoidal surface and a plane. Based on Hertzian contact theory, the semi-major axis a, semi-minor axis b, and the maximum Hertzian contact pressure p_H are obtained from the contact geometry, equivalent elastic modulus E', and applied normal load w.

To improve numerical stability and reduce the number of independent parameters, dimensionless variables are introduced for coordinates, density, viscosity, film thickness, and pressure, as follows:

$$X = \frac{x}{a},\ Y = \frac{y}{a},\ \rho^* = \frac{\rho}{\rho_0},\ \eta^* = \frac{\eta}{\eta_0},\ H = \frac{hR_x}{a^2},\ P = \frac{p}{p_H} \tag{1}$$

where x and y are the physical coordinates in the rolling and transverse directions, respectively; X and Y are the corresponding dimensionless coordinates; ρ and ρ_0 are the pressure-dependent lubricant density and the reference density, respectively; η and η_0 are the pressure-dependent lubricant viscosity and the reference viscosity, respectively; h is the local film thickness; R_x is the equivalent radius of curvature in the rolling direction; p is the local hydrodynamic pressure in the lubricant film; and E' is the equivalent elastic modulus. Using these dimensionless variables, the governing equations of the EHL problem are written as follows.

Dimensionless Reynolds equation:

$$\frac{\partial}{\partial X}\left(\varepsilon\frac{\partial P}{\partial X}\right) + \frac{\partial}{\partial Y}\left(\varepsilon\frac{\partial P}{\partial Y}\right) = \frac{\partial\left(\rho^* H\right)}{\partial X} \tag{2}$$

where

$$\varepsilon = \frac{\rho^* H^3}{\eta^* \lambda},\ \lambda = \frac{12U^* E' R_x^3}{p_H a^3}$$

In these expressions, ε is the dimensionless flow coefficient, λ is the dimensionless speed-related parameter, and U^* denotes the dimensionless velocity component in the x-direction.

Dimensionless boundary conditions:

$$\begin{cases} P(X_0,Y) = P(X_e,Y) = P(X,Y_0) = P(X,Y_e) = 0 \\ P(X,Y) \geq 0, X_0 < X < X_e, Y_0 < Y < Y_e \end{cases} \tag{3}$$

where X_0, X_e, Y_0 and Y_e define the inlet, outlet, and lateral boundaries of the computational domain in the dimensionless coordinate system. The pressure is set to zero at the domain boundaries, and negative pressure is not allowed.

Dimensionless film thickness equation:

$$H(X,Y) = H_0 + \frac{X^2 + e_k Y^2}{2} + P_{tr}\int_{X_0}^{X_e}\int_{Y_0}^{Y_e} \frac{P(\xi,\varsigma)}{\sqrt{(X-\xi)^2 + (Y-\varsigma)^2}} d\xi d\varsigma \tag{4}$$

where H_0 is the dimensionless central film thickness, and ξ and ζ are integration variables in the dimensionless computational domain. The ellipticity ratio e_k and the elliptical-contact deformation coefficient P_{tr} are defined as

$$P_{tr} = \frac{2p_H R_x}{E' \pi a},\ e_k = \frac{R_x}{R_y}$$

where R_y is the equivalent radius of curvature in the transverse direction.

Dimensionless viscosity–pressure relationship:

$$\eta^* = \exp\left[\left(\ln\eta_0 + 9.67\right)\left(\left(1 + 5.1\times10^{-9} p_H P\right)^Z - 1\right)\right] \tag{5}$$

where Z is the pressure–viscosity index in the Roelands pressure–viscosity relationship.

Dimensionless density–pressure relationship:

$$\rho^* = 1 + \frac{0.6\times10^{-9} p_H P}{1 + 1.7\times10^{-9} p_H P} \tag{6}$$

Dimensionless load balance equation:

$$\int_{X_0}^{X_e}\int_{Y_0}^{Y_e} P(X,Y)dXdY = \frac{2\pi b}{3a} \tag{7}$$

2.2.2 Numerical solution procedure

A coupled pressure-iteration and load balance strategy is used to solve the dimensionless EHL equations presented in Section 2.2.1. The overall procedure is shown in Figure 2.

For given input parameters, the contact geometry and maximum Hertzian contact pressure are first calculated. The elastic influence coefficient matrix is then constructed, and the convolution is accelerated using the fast Fourier transform. The film thickness and fluid properties are initialized based on an initial pressure distribution.

Starting from this initialized state, the solution is obtained using a nested iterative scheme. In the inner loop, the central film thickness is fixed and the Reynolds equation is solved using the Gauss–Seidel method to update the pressure field. After each update, the film thickness and fluid properties are recalculated based on the current pressure distribution until the pressure convergence criterion is satisfied. After the inner loop has converged, the outer loop is performed to enforce load balance. The load error is evaluated from the pressure distribution, and a relaxation strategy is used to update the central film thickness H_0 until the target load is reached. The solution is considered to have converged once both the pressure variation and load error fall below the prescribed tolerances, and then the pressure distribution and film thickness are obtained. Due to symmetry about the centreline, only half of the domain is computed, and the full-field solution is reconstructed by mirror extension, which reduces computational costs.

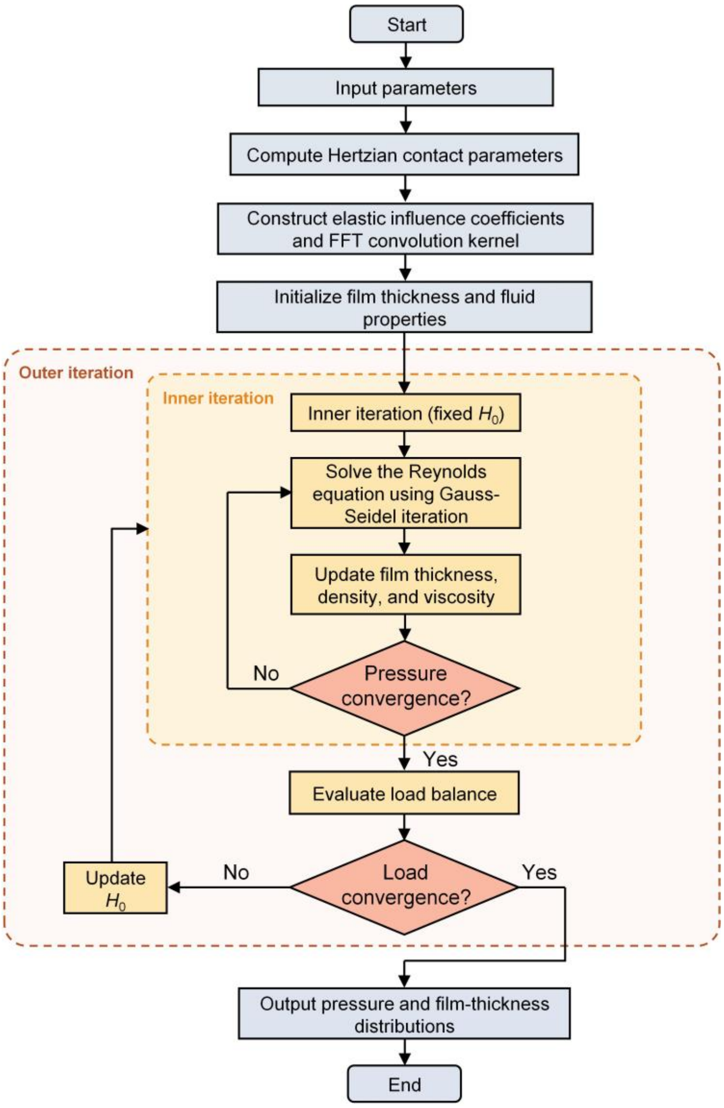

Figure 2: Flowchart of the numerical solution procedure.

2.3 Dataset generation

Direct prediction of full two-dimensional EHL fields is possible, but the output dimensionality increases rapidly with the grid resolution, leading to increased data requirements and training cost. For wheel–rail adhesion analysis under wet conditions, the centreline profiles of pressure and film thickness can capture the main EHL features of interest, such as pressure peaks and the inlet-to-outlet variation in film thickness. Therefore, this study predicts these centreline profiles instead of the full two-dimensional fields, thereby reducing the output dimension while retaining the main response features relevant to rapid adhesion analysis.

The dataset is generated within a two-parameter space defined by axle load and train speed. The axle-load range is 14–28 ton, and the speed range is 50–300 km/h. Latin hypercube sampling is employed to generate the samples. A linear scale is used for axle load, while speed is sampled on a logarithmic scale to provide balanced coverage over the broad speed range.

To ensure the reliability of the dataset, only samples satisfying the following conditions are retained: the pressure convergence error is below 1×10^{-5}, the load error is below 1×10^{-4}, and the pressure remains finite and non-negative, and the film thickness remains finite and positive. As shown in Figure 3(a), the invalid samples are mainly located in the low-load–high-speed region , especially when the axle load is below 20 ton and the speed exceeds 200 km/h. This trend is further confirmed by the failure probability distribution shown in Figure 3(b). This indicates that the numerical solver converges less reliably under these conditions, so such samples are excluded from the final dataset. To improve computational efficiency, the samples are solved in parallel batches on an AMD Ryzen 9 9950X CPU using 14 cores. A total of 600 valid samples are obtained.

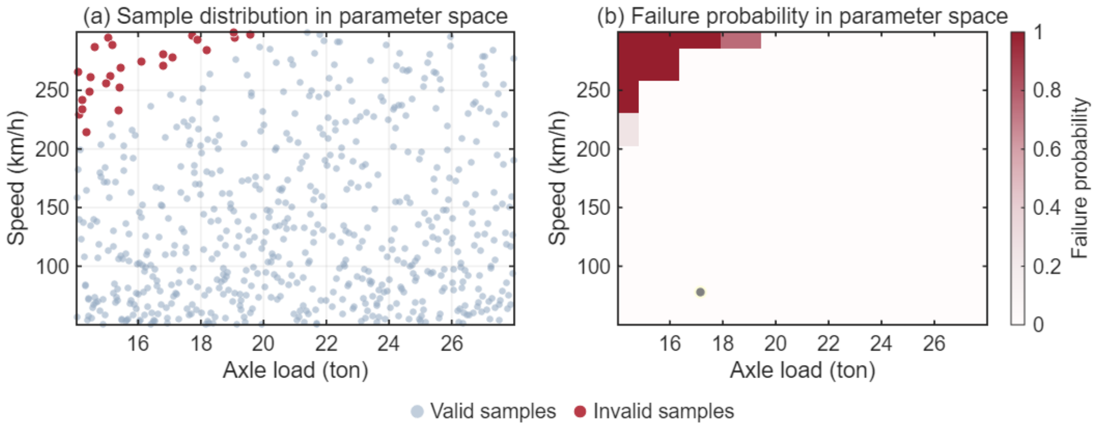

Figure 3: Sample distribution and convergence characteristics in the axle-load–speed parameter space: (a) sample distribution; (b) failure probability distribution.

2.4 MLP-based surrogate model

The dataset generated by the high-fidelity numerical model is used to train the surrogate models. The prediction task is formulated as a multi-output nonlinear regression problem, where the operating parameters are mapped to the corresponding centreline response distributions. Because pressure and film thickness differ in their scales and nonlinear response characteristics , two output-specific MLP models are used. As shown in Figure 4, the film-thickness model has two hidden layers with 64 neurons each, whereas the pressure model uses four hidden layers with 512, 256, 128, and 64 neurons, respectively.

Before training, the input parameters and output profiles are preprocessed to improve training stability and reduce scale differences between variables. This step is particularly important for pressure prediction because the centreline pressure profile contains sharp local peaks and a wide range of values between the low-pressure inlet/outlet regions and the high-pressure contact region. Therefore, the original 257-point pressure profile is downsampled to 129 points to reduce the output dimension while retaining the main profile shape. A logarithmic transformation is then applied to compress the pressure range and reduce the excessive contribution of high-pressure regions to the training loss:

$$P_{\log} = \log(P + \varepsilon) \tag{8}$$

where $\varepsilon = 10^{-6}$ is introduced to avoid taking the logarithm of zero.

In contrast, the film-thickness profile varies more smoothly along the centreline and does not contain pressure-like sharp spikes. Therefore, the original 257-point film-thickness profile is retained. The input variables and processed output profiles are then normalized using z-score normalization based on the statistics of the training set. The normalization parameters obtained from the training set are kept fixed when applied to the validation and test sets, thereby avoiding data leakage.

The samples are randomly partitioned into training, validation, and test sets in an 80%/10%/10% split, and use a fixed random seed throughout to ensure reproducibility. Model training is carried out with the scaled conjugate gradient algorithm, using the mean squared error as the loss in normalized space. The maximum number of epochs is set to 2000 for film-thickness prediction and 5000 for pressure prediction. After inverse normalization and inverse transformation, the prediction accuracy is assessed in the original output space using the mean absolute error (MAE).

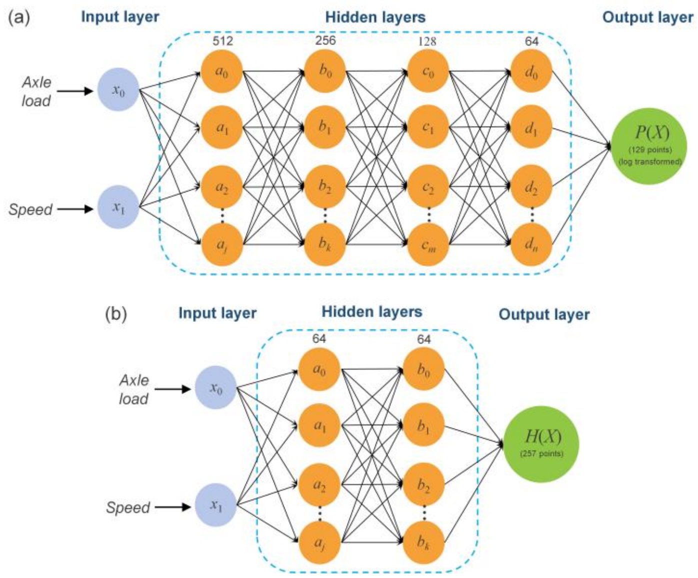

Figure 4: Network structures of the two output-specific MLP models for centreline response prediction: (a) pressure; (b) film thickness.

3 Results

3.1 Centreline EHL responses under representative operating conditions

Figure 5 compares the centreline pressure and film thickness distributions for three representative operating conditions, namely medium-load–medium-speed, low-load–high-speed, and high-load–low-speed. These cases are selected to cover representative regions of the load–speed parameter space and are used here to examine the characteristic pressure and film-thickness responses.

In all three cases, the pressure profiles show features commonly reported in EHL pressure distributions, including a primary pressure peak in the contact region and a secondary pressure spike near the outlet [16]. The pressure is low in the inlet region, increases towards the contact zone, and reaches the primary peak before decreasing sharply near the outlet. The secondary spike is smaller than the primary peak, and its position and shape vary with the operating conditions.

The film-thickness distributions vary more smoothly. The film is relatively thick in the inlet region and gradually decreases along the rolling direction. Within the contact zone, a nearly flat plateau is observed, followed by a distinct outlet constriction that determines the minimum film thickness, after which the film recovers downstream.

The influence of load and speed is also evident. Under low-load–high-speed conditions, the outlet pressure spike becomes more pronounced. In contrast, under high-load–low-speed conditions, the overall film thickness is lower, which is consistent with the reduced entrainment effect at low speed and stronger compression under high load. These results show that the numerical model can provide representative EHL solutions for wheel–rail contact under different operating conditions, providing physically meaningful data for subsequent surrogate-model training.

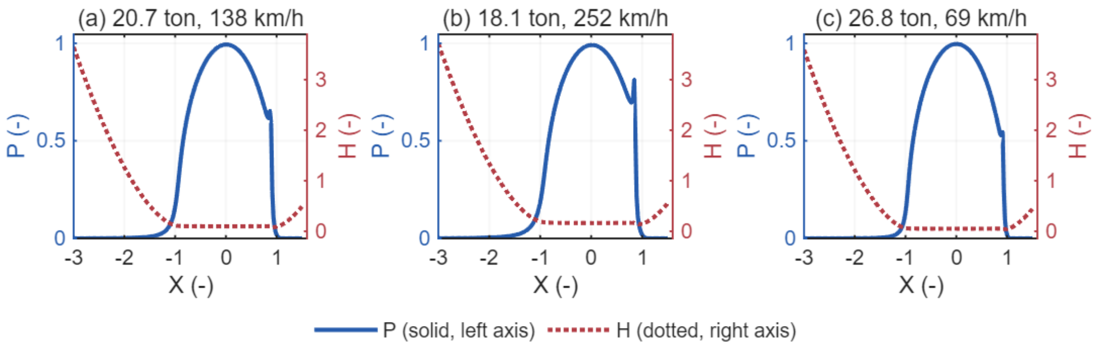

Figure 5: Dimensionless centreline pressure and film-thickness distributions under three representative operating conditions: (a) medium-load–medium-speed condition (20.7 ton, 138 km/h); (b) low-load–high-speed condition (18.1 ton, 252 km/h); and (c) high-load–low-speed condition (26.8 ton, 69 km/h). X, P, and H denote the dimensionless coordinate, pressure, and film thickness, respectively.

3.2 Prediction accuracy under representative operating conditions

Figure 6 shows a comparison between numerical solutions and MLP predictions for the dimensionless centreline responses under three representative operating conditions, including medium-load–medium-speed, low-load–high-speed, and high-load–low-speed.

For pressure prediction, the model accurately reproduces both the primary peak within the contact zone and the secondary spike near the outlet, even in cases with strong local gradients. For film thickness prediction, the predicted curves follow the overall trend along the centreline, capturing the decrease in the inlet region, the plateau in the contact zone, and the outlet constriction.

The MAE values range from 3.44×10^{-5} to 3.50×10^{-4} for the representative cases, indicating a low prediction error overall. As indicated by the MAE values annotated in Figure 6, relatively larger errors occur in the low-load–high-speed and high-load–low-speed cases, whereas the medium-load–medium-speed case is predicted more accurately. Nevertheless, the MLP predictions remain in close agreement with the numerical solutions, showing that the surrogate model can reproduce the main EHL response features under different operating conditions.

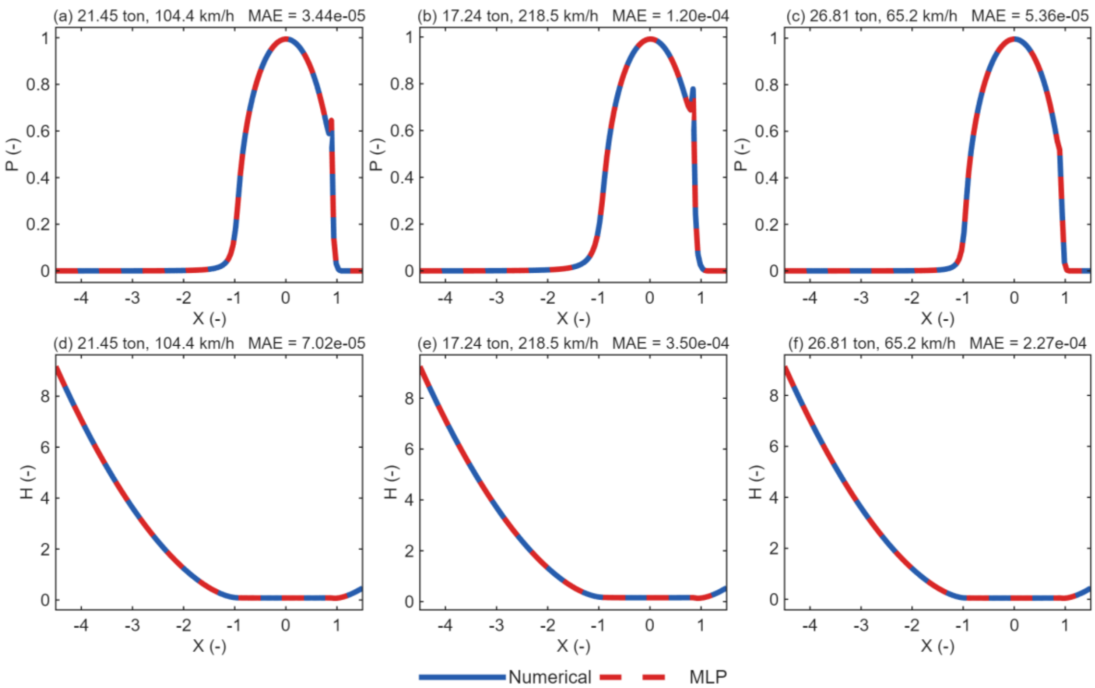

Figure 6: Comparison between numerical solutions and MLP predictions for the dimensionless centreline responses under three representative operating conditions: (a)–(c) pressure distributions; (d)–(f) film-thickness distributions. *X*, *P*, and *H* denote the dimensionless coordinate, pressure, and film thickness, respectively.

3.3 Generalization in the axle-load–speed parameter space

Figure 7 shows the MAE distribution of the test samples in the axle-load–speed parameter space, illustrating the predictive performance of the surrogate model under unseen operating conditions.

For both pressure and film thickness prediction, the errors for most test samples remain within a low range across the parameter space. As shown in Figure 7, no obvious regions of concentrated high error can be identified. For pressure prediction, most MAE values are below 1.5×10^{-4}, with only a few samples approaching 3×10^{-4}. These cases occur mainly in the high-load–low-speed and low-load–high-speed regions, but they are sparse and do not form distinct clusters. For film thickness prediction, most MAE values are below 5×10^{-4}, while a few cases approach 7×10^{-4}, particularly under high-load–low-speed and medium-load–low-speed conditions. These relatively larger errors therefore tend to occur near the boundary regions of the load–speed parameter space, especially in low-speed regions, which is consistent with the representative cases discussed in Section 3.2.

Film-thickness prediction exhibits slightly larger errors than pressure prediction. This difference may be partly attributed to the different preprocessing strategies and network structures used for the two outputs. The pressure model benefits from output reduction through downsampling and logarithmic transformation, whereas the film-thickness model directly predicts the higher-dimensional film-thickness outputs using a simpler network structure. Despite this, the overall error level remains low, and the surrogate model performs well across the parameter space.

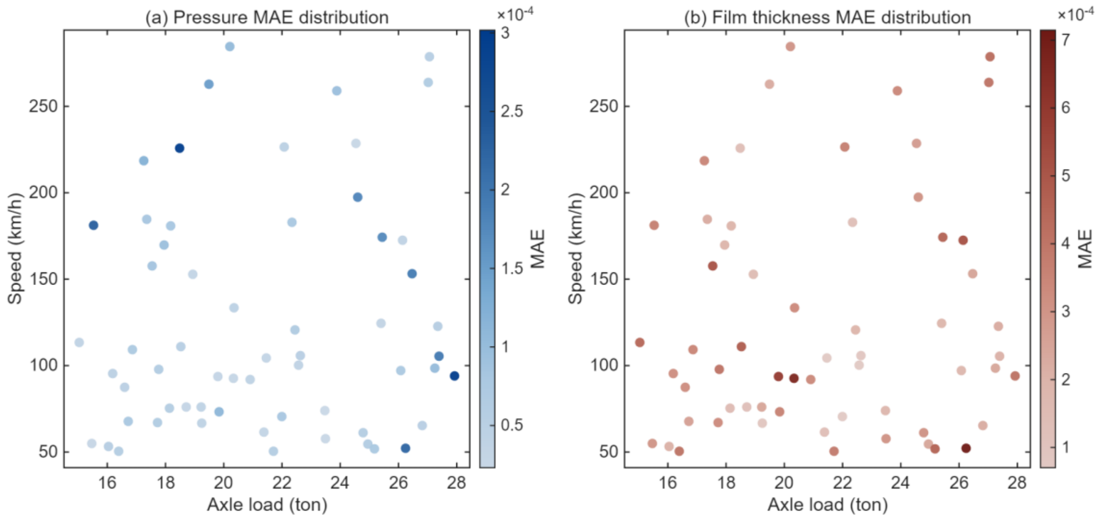

Figure 7: MAE distribution of test samples in the axle-load–speed parameter space: (a) pressure prediction; (b) film thickness prediction.

3.4 Statistical analysis of prediction errors

Although the absolute prediction errors are small, their distributions are analysed to assess the robustness of the surrogate model over the entire test set. Complementing the spatial error distribution discussed in Section 3.3, the histograms and cumulative distribution functions (CDFs) in Figure 8 reveal the concentration, dispersion, and high-error tail of the prediction errors for pressure and film thickness.

From the histograms in Figure 8(a)–(b), most samples have low MAE values, with only a limited number extending to higher values. For pressure prediction, the errors are relatively concentrated, with the main peak located roughly between 0.45×10^{-4} and 0.7×10^{-4}, and most remaining samples also lying within the lower-error range. In contrast, film thickness errors are more dispersed, with a broader distribution mainly between 2.24×10^{-4} and 3.4×10^{-4} and a small number of samples appearing at higher error levels.

The CDFs in Figure 8(c)–(d) provide a more direct comparison of the overall error levels. For pressure, the 90th and 95th percentiles of the MAE are below 1.86×10^{-4} and 2.29×10^{-4}, respectively. For film thickness, the corresponding values are 4.72×10^{-4} and 5.54×10^{-4}. This difference suggests that film-thickness prediction has slightly larger errors than pressure prediction in terms of MAE magnitude.

Together with the spatial error analysis in Section 3.3, these statistical results indicate that the relatively larger errors correspond to only a small portion of the test samples and are mainly associated with boundary regions or more extreme operating conditions. Even so, most samples still fall within a relatively low error range, and the model performance remains stable overall.

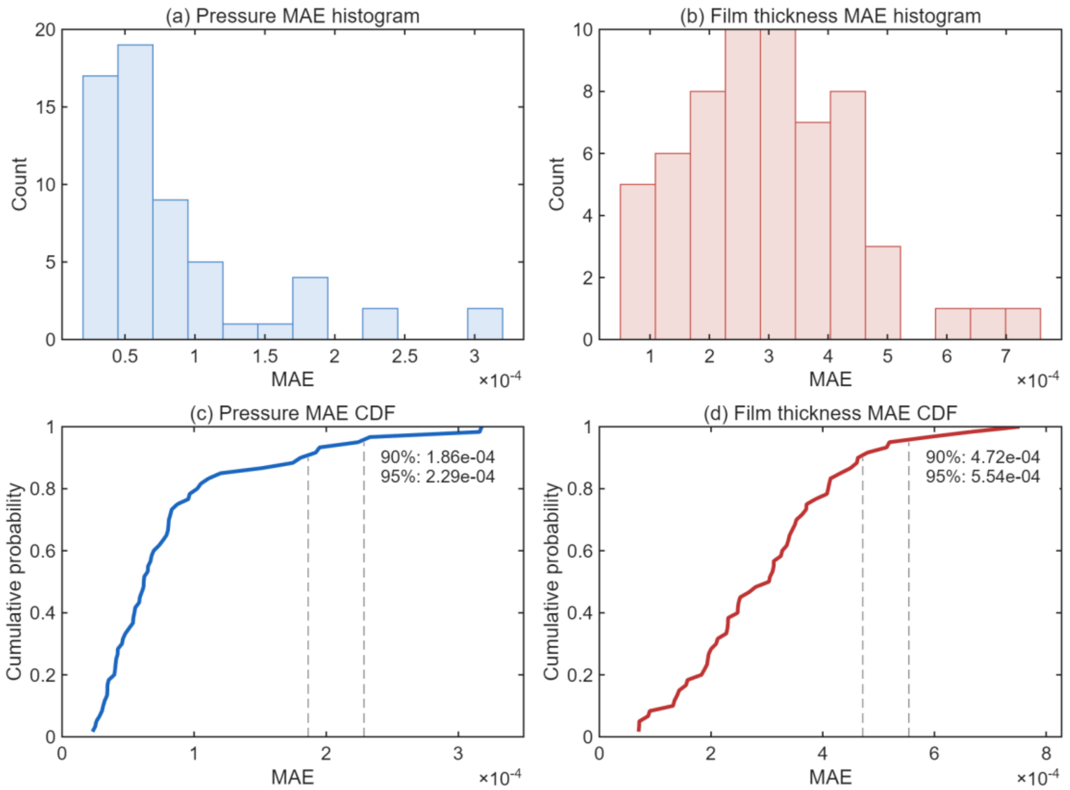

Figure 8: MAE distributions for pressure and film thickness prediction: (a) pressure histogram; (b) film-thickness histogram; (c) pressure CDF; (d) film-thickness CDF.

3.5 Computational cost and speed-up

Figure 9 presents the average computation time per case for the serial solver, the parallel solver, and the MLP surrogate model. All tests were performed on the same hardware/software platform (AMD Ryzen 9 9950X CPU, MATLAB R2025b), and the results are based on 10 operating conditions randomly selected from the test set. For the serial solver, the average time per case is defined as the mean computation time obtained by solving each case independently in sequence. For the parallel solver, the average time per case is calculated as the total wall-clock time required to solve the 10 cases in parallel divided by the number of cases. For the MLP model, the inference time per case, including both pressure and film-thickness predictions, is obtained by averaging over 1000 repeated predictions. The reported time for the parallel solver does not include initialization overhead.

The average computation time per case is 71.95 s and 38.81 s for the serial and parallel solvers, respectively, whereas the MLP surrogate model requires approximately 0.0056 s per case, corresponding to speed-up factors of approximately 1.27×10^4 and 6.87×10^3 relative to the serial and parallel solvers, respectively. These results demonstrate that the surrogate model is well suited for rapid evaluation under multiple operating conditions in wheel–rail adhesion analysis.

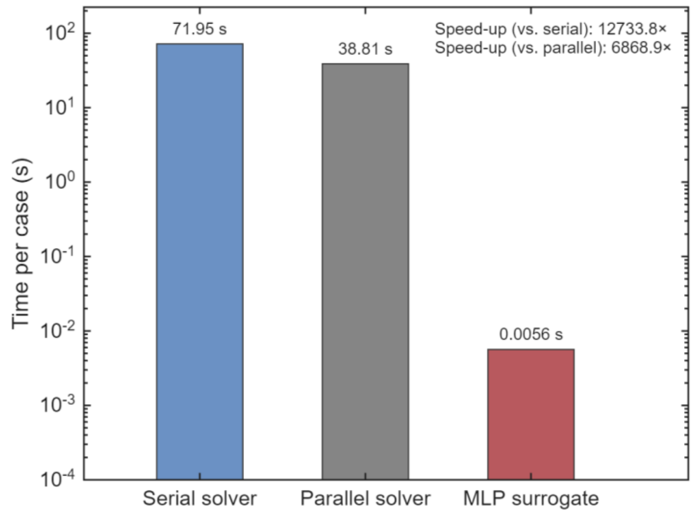

Figure 9: Average computation time per case for the serial solver, parallel solver, and MLP surrogate model.

4 Conclusions and Contributions

To address the high computational cost of numerical solutions in elastohydrodynamic lubrication of wheel–rail contact and the resulting difficulty in achieving rapid evaluation, an MLP-based surrogate framework is developed for efficient prediction of centreline pressure and film-thickness distributions. The results demonstrate that the surrogate framework reproduces the main features of high-fidelity numerical solutions under representative operating conditions, including pressure peaks and film-thickness variations. Over the test set, the prediction errors remain low in most cases, with slightly larger deviations mainly occurring near boundary or more extreme operating conditions. In addition, the computation time is reduced from seconds to milliseconds, corresponding to speed-up factors of approximately 1.27×10^4 and 6.87×10^3 relative to the serial and parallel numerical solvers, respectively.

This study demonstrates the potential of data-driven surrogate modelling for rapid and physically consistent approximation of wheel–rail EHL responses over a practical load–speed range. Future work could extend the present framework by incorporating tangential contact models for adhesion-curve prediction and by considering the effects of surface roughness and thermal factors under more complex operating conditions.

Acknowledgements

The authors gratefully acknowledge the financial support provided by the National Key Research and Development Program of China (Key Project of Transportation Equipment and Intelligent Transportation Technology, Grant No. 2024YFB4303300).

References

[1] M. Xu, W. Wang, X. Song, et al., "Research Progress on Friction Models of Wheel-rail Interface and Adhesion Control Technologies", Surface Technology, 54(13), 1–15, 2025.

[2] X. Song, S. Zhang, M. Xu, et al., "Experimental investigation on dynamic adhesion characteristics of wheel-rail under various media conditions at a large slip ratio range", Wear, 580–581, 206217, 2025.

[3] J. Zhou, W. Zhu, C. Tian, et al., "Experimental investigation of wheel rail adhesion under leaf contamination conditions", International Journal of Rail Transportation, 13(5), 908–927, 2025.

[4] J. Zhou, M. Wu, C. Tian, et al., "Experimental investigation on wheel–rail adhesion characteristics under water and large sliding conditions", Industrial Lubrication and Tribology, 73(2), 366–372, 2021.

[5] T. Ma, C. Tian, M. Wu, et al., "A 4-Phase Combined Adhesion Threshold Algorithm for Wheel Slide Protection Systems in Rail Vehicles", Actuators, 13(2), 47, 2024.

[6] L. Pugi, G. Paolieri, M. Giorgetti, et al., "HIL testing of wheel slide protection systems: criteria for continuous updating and validation", Railway Engineering Science, 31(2), 108–121, 2023.

[7] J. Huang, B. Wu, G. Xiao, et al., "Numerical investigation of wheel-rail adhesion using a simplified three-dimensional model considering surface roughness and temperature", Lubrication Science, 36(2), 88–103, 2024.

[8] Q. Li, S. Y. Zhang, B. Wu, et al., "Analysis on the effect of starved elastohydrodynamic lubrication on the adhesion behavior and fatigue index of wheel-rail contact", Wear, 510–511, 204506, 2022.

[9] X. Wang, H. Hua, K. Peng, et al., "Study on the wheel/rail adhesion characteristic under water and oil conditions by using mixed lubrication model", Wear, 544–545, 205279, 2024.

[10] B. Wu, J. Huang, X. Su, "A novel non-Hertzian wheel-rail adhesion model under wet conditions considering surface roughness", Journal of Central South University, 32, 4092–4104, 2025.

[11] Z. Wang, B. Wu, J. Huang, et al., "Dynamic wheel–rail adhesion characteristics on wet curved tracks considering surface roughness", Physics of Fluids, 37(2), 022104, 2025.

[12] M. Marian, J. Mursak, M. Bartz, et al., "Predicting EHL film thickness parameters by machine learning approaches", Friction, 11(6), 992–1013, 2023.

[13] J. Issa, A. El Hajj, P. Vergne, et al., "Machine learning for film thickness prediction in elastohydrodynamic lubricated elliptical contacts", Lubricants, 11(12), 497, 2023.
[14] M. Tošić, M. Marian, W. Habchi, et al., "Application of machine learning for film thickness prediction in elliptical EHL contact with varying entrainment angle", Tribology International, 199, 109940, 2024.
[15] J. Kelley, V. Schneider, G. Poll, et al., "Enhancing practical modeling: a neural network approach for locally-resolved prediction of elastohydrodynamic line contacts", Tribology International, 199, 109988, 2024.
[16] J. Huo, J. Zhou, T. Li, et al., "Thermal EHL characteristics investigation on axle box bearings of railway vehicle based on slicing method", Shock and Vibration, 2019, 6981482, 2019.